Observations of the Transfer of Energy and Momentum to the Oceanic Surface Boundary Layer beneath Breaking Waves

Malcolm E. Scully and John H. Trowbridge

Applied Ocean Physics and Engineering Department, Woods Hole Oceanographic Institution, Woods Hole, Massachusetts

Alexander W. Fisher

Horn Point Laboratory, University of Maryland Center for Environmental Science, Cambridge, Maryland

ABSTRACT

Measurements just beneath the ocean surface demonstrate that the primary mechanism by which energy from breaking waves is transmitted into the water column is through the work done by the covariance of turbulent pressure and velocity fluctuations. The convergence in the vertical transport of turbulent kinetic energy (TKE) balances the dissipation rate of TKE at first order and is nearly an order of magnitude greater than the sum of the integrated Eulerian and Stokes shear production. The measured TKE transport is consistent with a simple conceptual model that assumes roughly half of the surface flux of TKE by wave breaking is transmitted to depths greater than the significant wave height. During conditions when breaking waves are inferred, the direction of momentum flux is more aligned with the direction of wave propagation than with the wind direction. Both the energy and momentum fluxes occur at frequencies much lower than the wave band, consistent with the time scales associated with wave breaking. The largest instantaneous values of momentum flux are associated with strong downward vertical velocity perturbations, in contrast to the pressure work, which is associated with strong drops in pressure and upward vertical velocity perturbations.

1. Introduction

Near the ocean's surface, most field observations of the dissipation rate of turbulent kinetic energy (TKE) in the presence of surface gravity waves exceed values expected based on rigid boundary layer scaling (Kitaigorodskii 1983; Agrawal et al. 1992; Anis and Moum 1995; Drennan et al. 1996; Terray et al. 1996; Gemmrich 2010). It is traditionally assumed that the elevated rates of dissipation are the result of the convergence in the vertical transport of TKE driven by breaking waves, but there are no field observations that close the TKE balance in the presence of breaking waves to our knowledge. Turbulence closure models that account for wave breaking typically include a surface flux of TKE and assume that the vertical flux of TKE can be modeled as a downgradient process (Craig and Banner 1994; Burchard 2001). While it has been suggested that the covariance of turbulent pressure and velocity fluctuations (''pressure work'') plays an important role in the vertical transport of TKE (Janssen 1999), no oceanographic field observations of pressure work have been made in the surface boundary layer.

In addition to transferring mechanical energy, breaking waves transfer momentum from the wind into the ocean (e.g., Melville 1996). Mitsuyasu (1985) and Rapp and Melville (1990) have suggested that under strong forcing the majority of the air–sea momentum flux is transferred by breaking waves, but few observational studies have directly measured both the air- and waterside momentum fluxes under these conditions (Gerbi et al. 2008).

In this paper we use direct covariance measurement of turbulent fluxes to demonstrate that under breaking waves 1) the elevated rates of TKE dissipation are the result of the vertical convergence in TKE transport

---

driven primarily by pressure work; 2) the direction of momentum flux in the surface mixed layer is in the direction of wave propagation instead of the wind direction; 3) the fluxes of both momentum and energy occur at frequencies below the wave band and are consistent with the frozen-turbulence hypothesis; and 4) the largest instantaneous values of momentum flux are associated with strong downward vertical velocity perturbations, in contrast to the pressure work, which is associated with strong drops in pressure and upward vertical velocity perturbations.

2. Methods

The data presented below were collected over the course of 1 month during the fall of 2013 in Chesapeake Bay. This period was characterized by relatively energetic winds, including a prolonged nor'easter, during which winds exceeded $7\,\mathrm{m\,s^{-1}}$ for over 7 days, significant wave height H_s exceeded 1 m, and the dominant wave period reached 4 s (Scully et al. 2015). The focal point of the experiment was an instrumented turbulence tower that was deployed in 14 m of water, 8 km north of Cove Point, Maryland. Six Nortek vector acoustic Doppler velocimeters (ADVs) with pressure sensors were arrayed vertically at 2-m intervals on the tower, spanning the region from 1.5 m below the mean water surface to 2 m above the seafloor. The ADV sensor heads were mounted in a downward-looking orientation at the end of poles that extended out approximately 1 m from the tower perpendicular to the primary axis of the along-channel tidal flow [see Scully et al. (2015) or Fisher et al. (2015) for details]. The instrument housings were mounted on the poles away from the sensor head to minimize flow disturbance. The pressure sensors, which are located in the end cap of the instrument housings, were approximately 25 cm from the sampling volume of the ADVs. Immediately adjacent to the tower was a bottom-mounted tripod with an additional ADV whose sampling volume was located 0.7 m above the sea bed. All of the ADVs sampled at 32 Hz and collected 28 min of data every half hour, yielding nearly continuous velocity and pressure data.

A Campbell Scientific CSAT3 ultrasonic anemometer was mounted to the top of the tower and was used to make direct covariance estimates of the atmospheric momentum flux (wind stress). The sonic anemometer sampled the 3D velocity field and air temperature at 10 Hz continuously and was located 2.82 m above the mean sea surface. The atmospheric velocity cospectra were calculated using a 30-min block-averaging window, and Reynolds stress components were estimated by integrating the observed cospectra for frequencies less than 2 Hz (Rieder et al. 1994). Because of the sensitivity of flux measurements to

small variations in vertical velocity, the orientation of the sonic anemometer was tested and corrected using a planar fit method (Wilczak et al. 2001). This correction was performed on daily subranges of the data prior to flux calculations, as described in Fisher et al. (2015). The sonic anemometer was deployed 5 days after the tower, limiting the period when direct atmospheric and oceanic turbulence measurements were available to Julian days 269–291.

In the water column, the ADV data are used to estimate the dominant terms in the TKE budget, which for a horizontally homogeneous flow at steady state in the Boussinesq approximation can be written as (e.g., McWilliams et al. 1997):

$$-\overline{u_i'w'}\frac{\partial U_i}{\partial z} - \overline{u_i'w'}\frac{\partial U_{Si}}{\partial z} - \frac{g}{\rho_0}\overline{\rho'w'}$$
$$-\frac{\partial}{\partial z}\left(\frac{1}{2}\overline{u_j'^2 w'} + \frac{1}{\rho_0}\overline{p'w'}\right) = \varepsilon. \tag{1}$$

In (1), the primes denote fluctuations; the overbar indicates time averaging (28-min burst); the coordinate system is defined so that x_1 and x_2 are horizontal and $x_3 = z$ is vertical, positive upward, with $x_3 = z = 0$ at the mean sea surface; the mean horizontal velocity is U_i; the corresponding Stokes drift velocity is U_{Si}; the horizontal components of fluctuating velocity are u_1' and u_2'; the vertical fluctuating velocity is $u_3' = w'$; p is the pressure and ρ_0 is the constant reference density; and summation over repeated indices is implied ($i = 1, 2$ and $j = 1, 2, 3$). The first and second terms on the left-hand side (lhs) of (1) are the mean Eulerian shear production P_u and the Stokes drift production P_S, respectively. The third term on the lhs of (1) is the buoyancy flux. The fourth term on the lhs is the vertical gradient of the sum of the turbulent TKE flux and the pressure work. Throughout this paper we refer to the term in parentheses (i.e., the sum of the turbulent TKE flux and pressure work) as the total TKE transport (denoted F in figures). For horizontally homogenous turbulence at steady state, the lhs is balanced by the dissipation rate of TKE ε, the only term on the right-hand side (rhs) of (1).

Estimates of ε are obtained from the inertial subrange of vertical velocity at frequencies higher than those of the observed surface waves (see Fig. A2 in the appendix). We use the method outlined in Gerbi et al. (2009), which accounts for the influence of unsteady advection by surface waves on the turbulent autospectra for frequencies higher than the wave band. The method of Gerbi et al. (2009) applies the model of Lumley and Terray (1983) including all three components of wave orbital motion, and is equivalent to the method outlined by Feddersen et al. (2007).

All of the terms on the lhs of (1) require covariance estimates of turbulent fluxes. When surface gravity waves

and turbulent motions occur within a similar frequency range, energetic orbital motions from the waves often contaminate covariance measurements of turbulent fluxes in the water column (Trowbridge 1998). To avoid this issue, the raw 32-Hz data are used to calculate the co-spectra between the vertical velocity and u_i', p', and $(1/2)u_j'^2 w'$, and the cospectra are integrated with respect to frequency to determine the turbulent fluxes, with the integration limited to frequencies less than $1/10$ Hz. In a fetch-limited environment such as Chesapeake Bay, this is well below the frequencies of the surface waves. This approach is justified by the following (see below): 1) the agreement between our estimates of momentum flux at $z \sim -1.5$ m and the magnitude of the observed wind stress, 2) our ability to close the TKE budget, and 3) the observed spectral gap between the frequency of the dominant surface waves and the dominant frequencies of momentum and energy flux. These methods provide direct covariance estimates of the vertical momentum flux, the turbulent TKE flux, and the pressure work at six vertical locations spanning the water column. We cannot directly estimate the buoyancy flux from the measurements that were obtained, but indirect estimates made from the surface heat flux (Scully et al. 2015) are at least two orders of magnitude smaller than the observed near-surface dissipation rates, so the buoyancy flux is not considered.

The mean shear $\partial U_i / \partial z$ on the lhs of (1) is estimated by differencing mean velocity measurements at the separate ADV elevations, and the corresponding Stokes drift shear is estimated following Kenyon (1969), using estimates of the directional wave spectrum $E_{\eta\eta}(\omega, \theta)$ obtained from the uppermost waterside velocity and pressure measurements [see Scully et al. (2015) for details], where ω is radian frequency and θ is direction.

A potential concern is that the pressure measurements used to estimate $\overline{p'w'}$ are compromised by dynamic pressures associated with flow disturbance around the sensors. As detailed in the appendix, our analysis suggests that our pressure measurements are not significantly degraded by flow disturbance because of the following: 1) the dynamic pressure, a plausible upper bound on the error associated with flow disturbance, is significantly smaller than the pressure fluctuations that create $\overline{p'w'}$; 2) estimates of the pressure error obtained by comparing the observed pressure fluctuations within the wave band with linear wave theory suggest that pressure errors in our data are at most $\sim 10\%$, which would not significantly impact our measurements of $\overline{p'w'}$; 3) Wyngaard et al. (1994) carefully considered the impact of pressure errors due to flow distortion and concluded that the errors were approximately 10% of the dynamic pressure, thus much smaller than the upper

bound; and 4) estimates of $\overline{p'w'}$ succeed in approximate closure of the TKE balance (see below), which seems unlikely if the pressure measurements were significantly impacted by flow distortion.

To aid the interpretation, we calculate the rate of energy input from the wind into the wave field F_0:

$$F_0 = g \int_0^{2\pi} \int_0^{\omega_{\max}} \beta E_{\eta\eta} \, d\omega \, d\theta, \qquad (2)$$

where β is the formulation of Donelan and Pierson (1987) for the e-folding scale for the growth rate of wave energy in the absence of nonlinear interactions and dissipation. Consistent with previous studies, we assume F_0 represents the energy flux into turbulence via wave breaking (Terray et al. 1996).

Because our interest is in the dynamics of the surface mixed layer under breaking waves, we limit our analysis to conditions when the observed wind speed is greater than $3 \, \mathrm{m \, s^{-1}}$ and the observed low-frequency pressure fluctuations exceed the instrument noise flow (see appendix). Approximately 58% of the data meet these criteria, with the majority of the data coming from the prolonged nor'easter from Julian days 280–287.

3. Results

Estimates of the magnitude of momentum flux from the near-surface ADV ($z \sim -1.5$ m) are consistent with the covariance estimates of the surface wind stress from the sonic anemometer on the tower (Figs. 1a,b). Under energetic wind forcing the measured stress profile decreases linearly to a depth of about 10 m (Fig. 1c). There is an increase near the bed associated with the bottom boundary layer, but the surface stress is over 3 times larger than the measured bottom stress, on average (Fig. 1c). Persistent near-bed salinity stratification often limits the vertical extent of the bottom boundary layer to the lowest several meters of the water column (Scully et al. 2015). The agreement between the magnitude of the low-frequency covariance estimates of momentum flux at $z \sim -1.5$ m and the atmospheric covariance measurements provides confidence that we are resolving nearly all of the vertical momentum flux in the water column.

During strong wind events there is evidence that air bubbles are advected to a depth of at least $z = -3.5$ m. These events are characterized by rapid increases in acoustic backscatter, intensified downward velocities, and increases in horizontal velocity in the direction of wave propagation (Fig. 2). The negative correlation between the downward and downwave velocity perturbations leads to a significant instantaneous momentum flux in the direction of wave propagation associated with
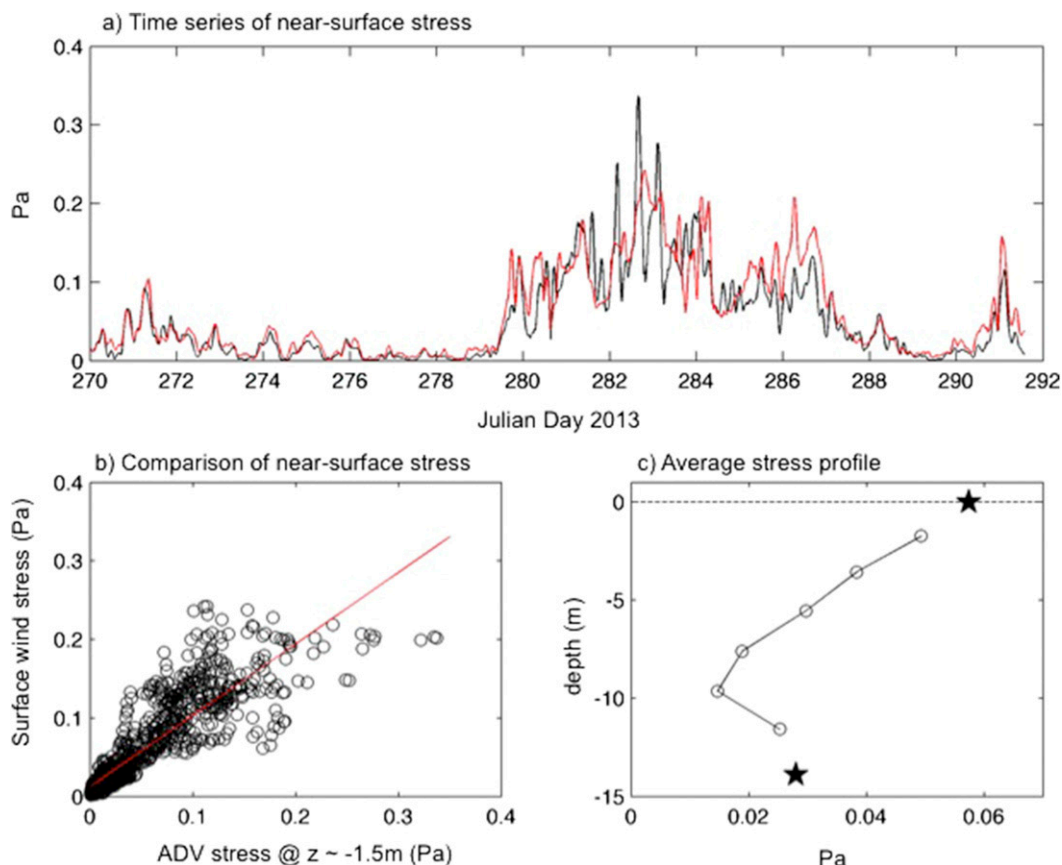
FIG. 1. (a) Comparison of the time series of the atmospheric surface wind stress measured ~2.8 m above the water surface by a sonic anemometer (red line), with the low-frequency momentum flux measured by the ADV ~1.5 m below the water surface (black line); (b) scatterplot of the same data with best-fit linear regression (slope = 0.91); (c) the stress profile averaged over all conditions where 10-m-adjusted wind speed exceeds $3 \, \mathrm{m \, s}^{-1}$. In (c) the circles represent the individual ADV locations on the tower, and stars represent the surface wind stress from the sonic anemometer and the bottom stress from the ADV deployed on a bottom lander adjacent to the tower.

these episodic events (Fig. 2c). The high backscatter events occur roughly every 2–3 min and are consistent with our observation that nearly all of the momentum flux is contained in the low-frequency covariance, well below the frequencies of the surface waves.

The observed momentum flux vector in the water column at $z \sim -1.5$ m is more aligned with the direction of wave propagation than the direction of the surface wind stress measured by the sonic anemometer (Fig. 3a). For conditions when the 10-m-adjusted wind speed is greater than $3 \, \mathrm{m \, s}^{-1}$, the direction of the momentum flux measured at $z \sim -1.5$ m is not significantly ($\alpha < 0.05$) different than the observed direction of the dominant surface waves. In contrast, significant differences are observed between the direction of momentum flux at $z \sim -1.5$ m and the observed wind direction (Fig. 3b). Our observations suggest that the waves at this site align more with the dominant axis of fetch than with the local wind direction (Scully et al.

2015). We observe no misalignment between the surface wind stress and the observed wind direction (Fig. 3c).

As with other field observations of TKE dissipation made in the water beneath surface waves, we document values of ε that significantly exceed wall layer scaling [$\varepsilon = u_*^3/(\kappa z)$, where u_* is the friction velocity, $\kappa \approx 0.40$ is von Kármán's constant, and z is the distance from the boundary] (Fig. 4a). The sum of the Eulerian and Stokes shear production from the uppermost pair of ADVs is more than an order of magnitude smaller than the observed dissipation. Observed values of ε are in excess of shear production in the upper water column, and a production–dissipation balance only holds for depths approaching the wavelength λ of the dominant surface waves (Fig. 4a). In the upper water column, the divergence in total TKE transport contributes significantly to the TKE balance, with a first-order balance between dissipation and the divergence of total TKE transport
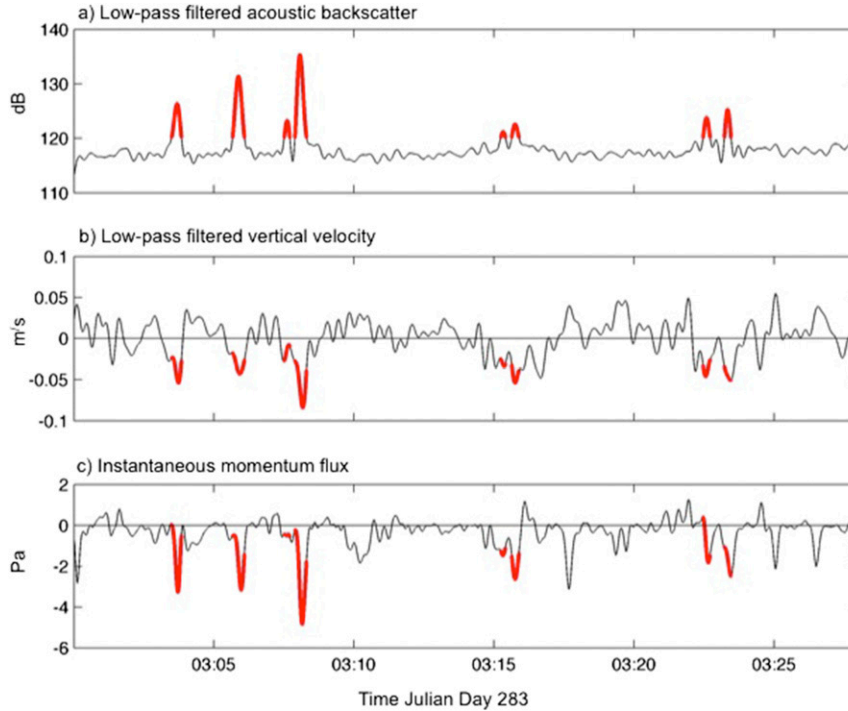
FIG. 2. Low-pass-filtered ($<1/10$ Hz) ADV data from $z \sim -3.5$ m on Julian day 283 when $H_s =$ 0.9 m, including (a) acoustic backscatter, (b) vertical velocity, and (c) instantaneous momentum flux calculated from the product of the vertical and horizontal (downwave) velocities. Periods of elevated backscatter (>120 dB) are indicated with the heavy red line, which we interpret as the downward advection of air bubbles. These periods coincide with large instantaneous momentum fluxes.

down to a depth of $z \sim -0.3\lambda$. Comparison of the average vertical profiles of dissipation with the sum of the Eulerian shear production, Stokes shear production, and the divergence of total TKE transport balance to within 20% at all depths (Fig. 4b).

To present all of the estimates from the water column TKE balance, we compare the rhs and lhs of (1), integrated from $z = -11.8$ m to $z = -1.5$ m. Because we are not measuring buoyancy flux, the rhs includes the integrated Eulerian shear production, the integrated
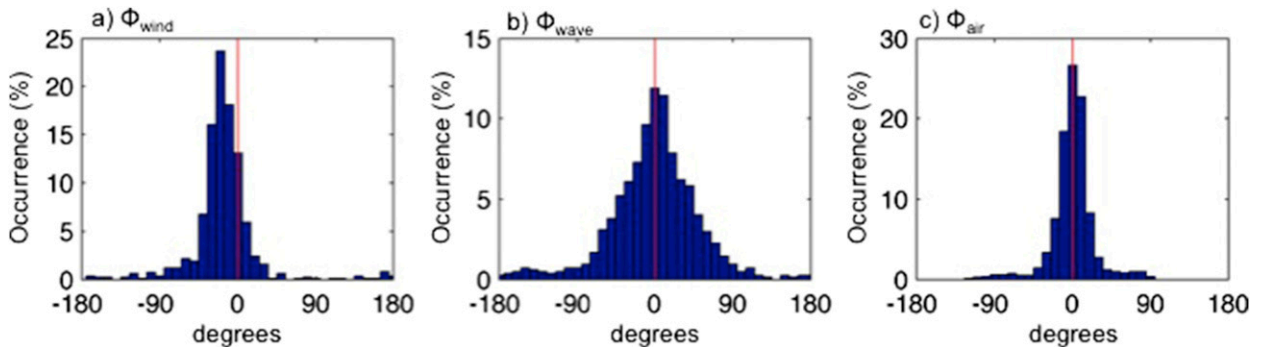

FIG. 3. (a) Misalignment ϕ_{wind} between the momentum flux measured in the water column at $z \sim -1.5$ m and the wind direction; (b) misalignment ϕ_{wave} between the momentum flux measured in the water column at $z \sim -1.5$ m and the wave direction; and (c) misalignment ϕ_{air} between the momentum flux measured in the atmosphere at $z \sim 2.8$ m and the wind direction. The mean values of $\phi_{wind} = -16 \pm 2.5°$ and $\phi_{wave} = -1.1 \pm 3.4°$ differ significantly at 95% confidence and suggest that the momentum flux in the water is more aligned with the wave field than with the local winds. Values of ϕ_{air} are not statistically different from zero ($0.3 \pm 1.7°$), indicating that the wind stress and wind direction are aligned at the measurement height.
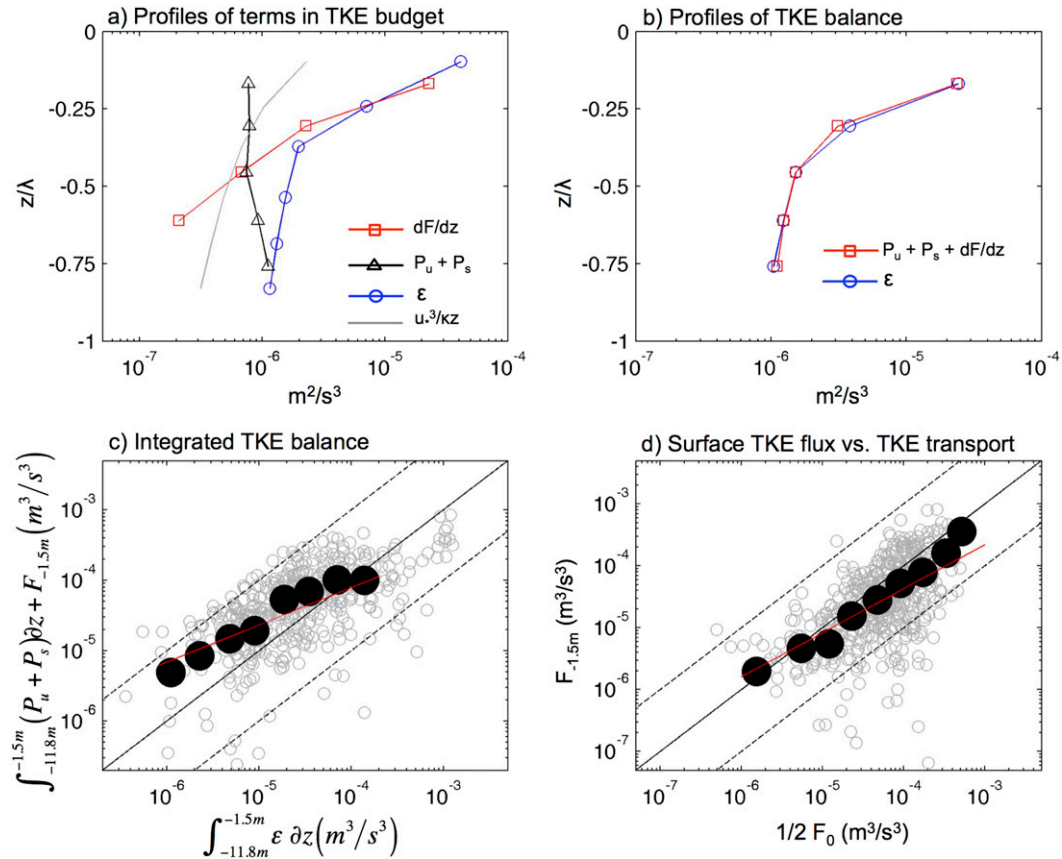
FIG. 4. (a) Average profiles for the terms in the TKE budget, including the dissipation rate of TKE ε (blue circles), the sum of the Eulerian shear production P_u and Stokes shear production P_S (black triangles), and the divergence in total TKE transport dF/dz, including both pressure work and turbulent TKE flux (red squares; negative values not shown). The gray line represents the wall layer estimate of dissipation $u_*^3/(\kappa z)$. (b) Average profiles of the dissipation rate of TKE (blue circles) and the sum of shear production and divergence in total TKE transport $(P_u + P_S + dF/dz)$ (red squares). (c) Comparison of $\int_{-11.8\,\mathrm{m}}^{-1.5\,\mathrm{m}} \varepsilon\, \partial z$ with $\int_{-11.8\,\mathrm{m}}^{-1.5\,\mathrm{m}} (P_u + P_S)\, \partial z + F_{-1.5\,\mathrm{m}}$. (d) Comparison of half the estimated surface flux of TKE F_0 with the total TKE transport at $z = -1.5$ m ($F_{-1.5\mathrm{m}}$). In both (c) and (d) the gray circles are the raw data, the black circles are bin-averaged data, and the red line is the least squares fit.

Stokes shear production, and the total TKE transport at $z = -1.5$ m (the transport at $z = -11.8$ m is negligible) (Fig. 4c). The total TKE transport at $z = -1.5$ m is nearly always directed downward, consistent with a source of TKE to the underlying water column that must be dissipated. Although there is significant scatter, there is a first-order balance between the integrated terms on the lhs of (1) and the integrated dissipation. The residual is less than 20% of the integrated dissipation, on average, suggesting that the dominant terms in the balance have been resolved. The downward transport of TKE, which is dominated by pressure work, is the largest source of TKE to the water column and is roughly an order of magnitude larger than the sum of the integrated Eulerian and Stokes shear production.

The conceptual model of Terray et al. (1996) assumes that dissipation is constant for depths shallower than H_s

and then varies as z^{-2} deeper in the water column. This model predicts that approximately half the dissipation occurs at depths less than H_s so that the downward flux of TKE at $z \sim -H_s$ is roughly half of the energy input at the surface by breaking waves. Estimates of total TKE transport from the upper ADV are generally consistent with half of the surface flux (F_0) as estimated via (2) (Fig. 4d). This is consistent with the results from the TKE balance and provides evidence that the dominant mechanism by which wave energy is transmitted deeper into the water column is the total TKE transport associated with breaking waves.

To provide a simple evaluation of the shapes of the cospectra that represent the downward transport of momentum, TKE, and air bubbles, we utilize the generalized two-parameter semiempirical model proposed by Kaimal et al. (1972), which can be represented as follows:
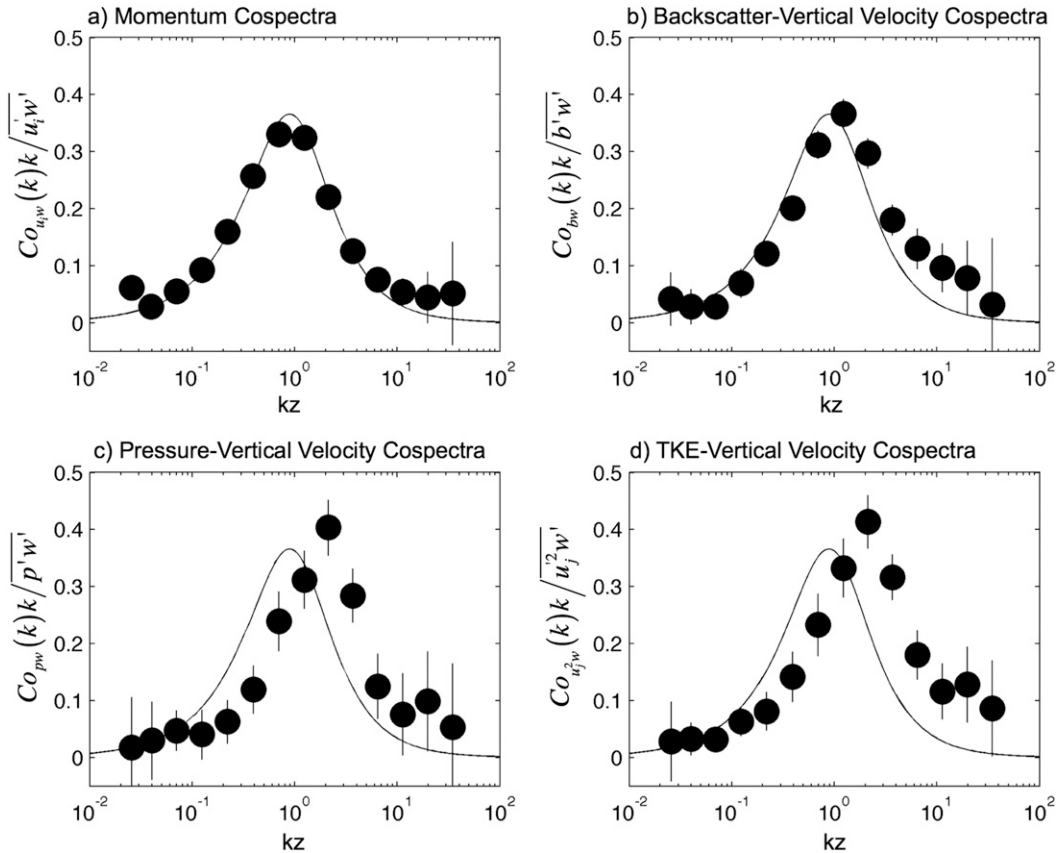
FIG. 5. Normalized covariance-preserving wavenumber cospectra of (a) momentum flux, (b) acoustic backscatter flux, (c) pressure work, and (d) turbulent TKE flux. The covariance-preserving cospectra are normalized by the low-frequency ($<1/10$ Hz) covariance, and wavenumber k, which is calculated employing Taylor's frozen-turbulence hypothesis and the observed current speed, is normalized by the distance from the boundary z. All the observed cospectra have been bin averaged as a function of kz, and vertical lines represent the 95% confidence interval assuming the error is normally distributed. The solid line is (3) in the text.

$$\mathrm{Co}_{\alpha w}(k) = A \overline{\alpha' w'} \frac{1/k_0}{1 + (k/k_0)^{7/3}}, \tag{3}$$

where α is a quantity of interest, $\overline{\alpha' w'}$ is the covariance, k is the streamwise wavenumber, k_0 is a rolloff wavenumber associated with the inverse of the dominant turbulent length scale, and the constant $A = 7/(3\pi) \sin(3\pi/7)$ is determined by requiring that the integral of the one-sided cospectrum equal the vertical flux. All of the observed cospectra qualitatively agree in shape with the Kaimal model (Fig. 5). In both the momentum cospectra and the cospectra of vertical velocity and acoustic backscatter (as a proxy for air bubbles), the peak of the variance-preserving cospectra occurs at wavenumbers that are consistent with the distance from the boundary $k \sim z^{-1}$ (Figs. 5a,b). Both the normalized $\overline{p' w'}$ and $(1/2)\overline{u_j'^2 w'}$ cospectra are generally consistent with the model as well, but the spectral peak occurs at wavelengths that equate to length scales smaller than the distance from the boundary,

suggesting that the transport of TKE is happening at smaller scales than the momentum flux (Figs. 5c,d).

Previous work in the atmospheric boundary layer (Wyngaard and Cote 1972) demonstrates that the peak of the variance-preserving cospectra for momentum occurs at $k \sim z^{-1}$ in the absence of a stabilizing surface heat flux. In this experiment, the majority of the data considered have a destabilizing heat flux and the Monin–Obukhov length L_m estimated from the surface heat flux is negative for $\sim$75% of the data. Only 3% of the data have $z/L_m > 0.2$, and we see no significant differences in the non-dimensionalized cospectra if we consider the data with $z/L_m < 0$ and $z/L_m > 0$ separately. Thus, in spite of the added complexity of breaking waves, the dominant length scale of the momentum-carrying motions beneath the sea surface is similar to the corresponding scale in the atmospheric boundary layer over a fixed surface.

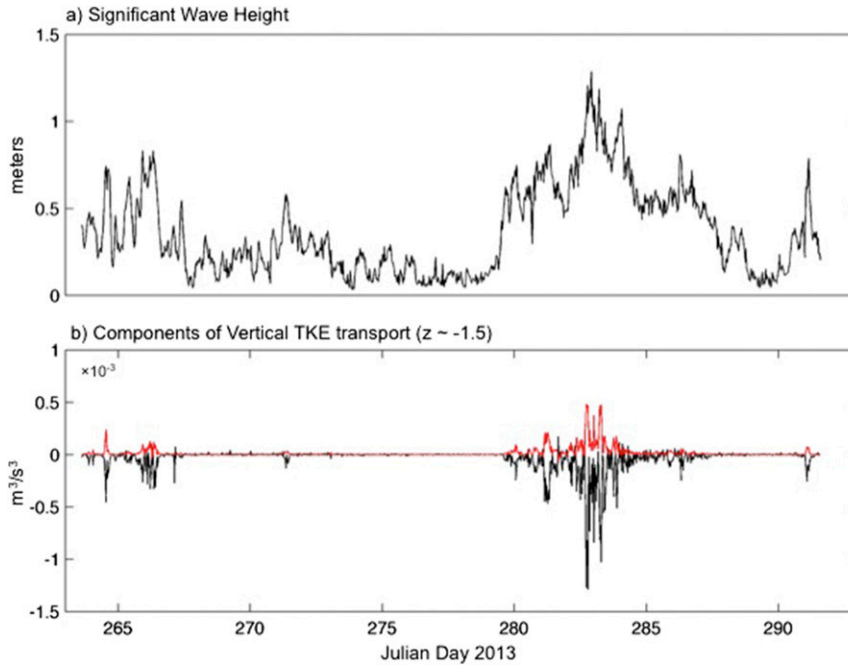Significant downward TKE flux in the water column only occurs during conditions of elevated wave energy

FIG. 6. (a) Significant wave height. (b) Components of total TKE transport, including pressure work (black line) and turbulent TKE flux (red line) measured from low-frequency covariance at $z \sim -1.5$ m.

(Fig. 6a). At $z \sim -1.5$ m the estimates of $\overline{p'w'}$ are almost always directed downward, while $(1/2)\overline{u_j'^2 w'}$ is directed upward (Fig. 6b). The overall magnitude of $\overline{p'w'}$ is roughly a factor of 4 greater than $(1/2)\overline{u_j'^2 w'}$, and, as a result, the total TKE transport is directed downward in the upper part of the water column and is accomplished by pressure work. The water column estimates of TKE decrease with distance from the surface, so the flux driven by $(1/2)\overline{u_j'^2 w'}$ is countergradient, consistent with

measurements in the convective atmospheric boundary layer (McBean and Elliott 1975).

Conditional averaging of the observed instantaneous low-frequency flux measurements demonstrates that the greatest momentum flux occurs during downward vertical velocity perturbations (Fig. 7a). These downward "sweeps" of high-momentum fluid contribute to the overall momentum flux more than the corresponding upward transport of low-momentum fluid. In contrast,
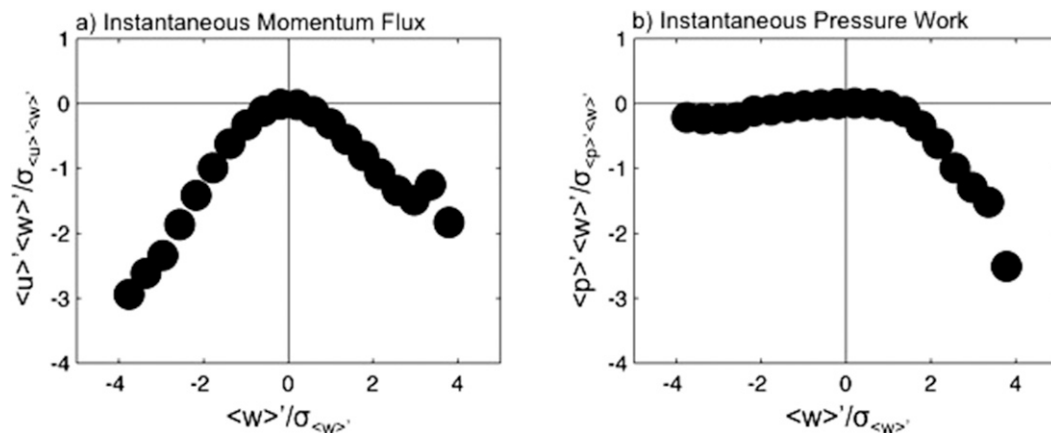

FIG. 7. (a) Instantaneous momentum flux and (b) instantaneous pressure work measured at $z \sim -1.5$ m and conditionally averaged as a function of the observed vertical velocity. Variables were low-pass filtered ($<1/10$ Hz; denoted by angled brackets) and normalized by the standard deviation for each burst prior to averaging.
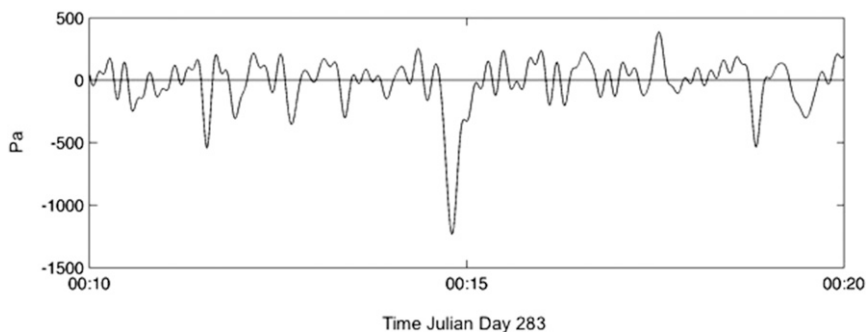
FIG. 8. Example of low-frequency (<1/10 Hz) pressure anomaly under strong wave forcing, showing strong drops in pressure and negative skewness.

the greatest pressure work is associated with large drops in pressure and upward vertical velocity fluctuations (Fig. 7b). Downward-directed vertical velocities are associated with positive pressure anomalies, on average, but their contribution to the total pressure work is much smaller than corresponding upward velocity perturbations of similar magnitude.

4. Discussion

Our results show that the pressure work is dominated by upward velocities, which coincide with strong decreases in pressure. Under strong wave forcing, data from the uppermost pressure sensor demonstrate strong intermittent pressure drops (Fig. 8) and negative pressure skewness (Fig. 9a). These pressure drops that dominate the pressure work are similar to laboratory measurements and numerical simulations that demonstrate strong intermittent pressure drops in a turbulent flow that are caused by tubelike vortical structures, which concentrate vorticity and result in negative pressure skewness (Douady et al. 1991; Metais and Lesieur 1992; Fauve et al. 1993; Abry et al. 1994; Cao et al. 1999). While the vortex tubes resolved by these studies are on the order of the Kolmogorov scale (She et al. 1990), Pizzo and Melville (2013) propose that deep-water wave breaking results in a much larger-scale U-shaped half vortex ring. The concentrated vorticity associated with this type of structure could result in the intermittent pressure drops that we observe and might explain the associated negatively skewed pressure probability density function (PDF) that is observed when wave forcing is strong (Fig. 9a), in contrast to the more nearly Gaussian distribution under weak wave forcing (Fig. 9b). The negative skewness is limited to conditions with strong wave forcing and to $z > -0.2\lambda$ (Fig. 9c), consistent with the depths of enhanced vorticity associated with breaking waves in the laboratory (Melville et al. 2002).

In the results presented above, the direction of the atmospheric momentum flux is closely aligned with the observed wind direction (Fig. 3c). Studies in open ocean environments have reported that the atmospheric stress vector measured above surface waves often lies between the wind direction and the direction of the underlying swell (Rieder et al. 1994; Grachev et al. 2003). The waves in Chesapeake Bay are fetch limited with no nonlocal swell, which may explain the close alignment between the wind and stress directions at the measurement location. The misalignment between the direction of the atmospheric and water column momentum flux estimates suggests there is a stress divergence in the unresolved region between the sonic anemometer and the uppermost ADV. Our measurements cannot determine if this stress divergence is in the uppermost part of the oceanic surface boundary layer or the lowermost part of the atmospheric boundary layer. Over most of the resolved portion of the water column, the direction of the momentum flux vector remains relatively constant with depth and aligned with the wave direction (Fig. 10). Only very near the bed does the momentum flux vector align with the local current direction (Fig. 10f). Chesapeake Bay has significant tidal currents, but at this location persistent near-bed salinity stratification limits the bottom boundary layer to a thin near-bed region.

The results from the TKE balance presented above are consistent with numerical simulations that include a stochastic parameterization for wave breaking (Sullivan et al. 2007; McWilliams et al. 2012). In these studies the effects of breaking surface waves are modeled by imposing randomly distributed horizontal accelerations near the ocean surface. These accelerations are imposed as an external force in the model, which generates an additional term in the TKE equation that is referred to as "breaker work." McWilliams et al. (2012) document that the production of TKE by the sum of the total TKE transport and breaker work is balanced by dissipation at first order. The sum of the breaker work and the total TKE transport term is more
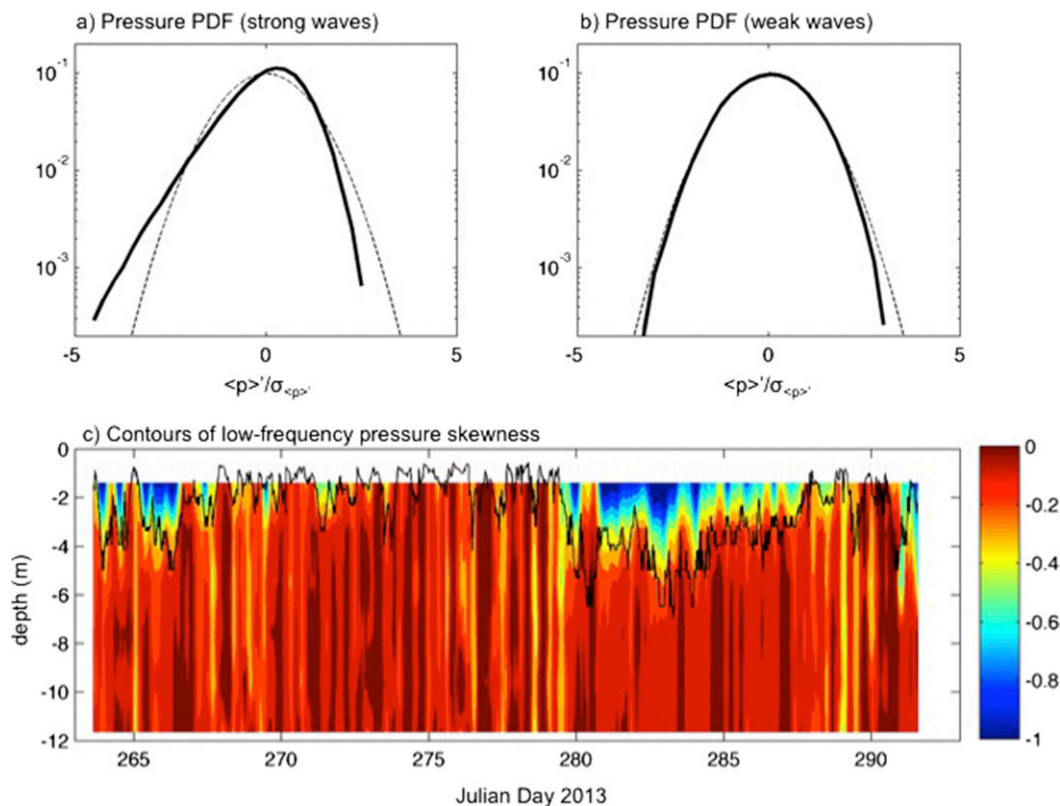
FIG. 9. Probability density function (PDF) of low-frequency ($<1/10$ Hz) pressure fluctuations from the pressure sensor $z \sim -1.5$ m, averaged over all bursts associated with the (a) upper quartile and (b) lower quartile of observed significant wave height, demonstrating negative skewness associated with strong wave forcing. Solid back line is the average PDF, and the dashed line represents a Gaussian distribution with zero mean and observed standard deviation. (c) Contours of low-frequency pressure skewness measured at all six locations along the tower. Negative skewness is limited to depths $> -0.2\lambda$, the depth limit of breaking-induced vorticity identified by Melville et al. (2002), which is indicated by the solid black line.

than an order of magnitude larger than the sum of the Eulerian and Stokes shear production, consistent with our results. We suggest that the breaker work that results from the imposed forcing in these modeling studies would appear as pressure work in field observations.

5. Conclusions

The results presented above provide evidence that the elevated dissipation rates that are commonly observed in the presence of breaking waves are the result of the convergence in the total TKE transport. Near the surface ($z > -0.3\lambda$) direct covariance measurements of the convergence in total TKE transport balance the observed dissipation at first order, and the downward flux of TKE at $z \sim -H_s$ is roughly half the estimated surface flux due to breaking waves. Our results demonstrate that pressure work is the primary mechanism by which energy is transferred from waves into turbulence. The observed direction of momentum flux measured in the water column near the ocean surface is more aligned with the observed wave direction than with the wind stress, providing field confirmation that breaking waves also play an important role in the exchange of momentum. Turbulent cospectra exhibit a clear spectral gap with the flux of energy and momentum occurring at frequencies much lower than the incident surface waves. These results demonstrate the dominant role that waves play in the flux of energy and momentum between the ocean and the atmosphere.
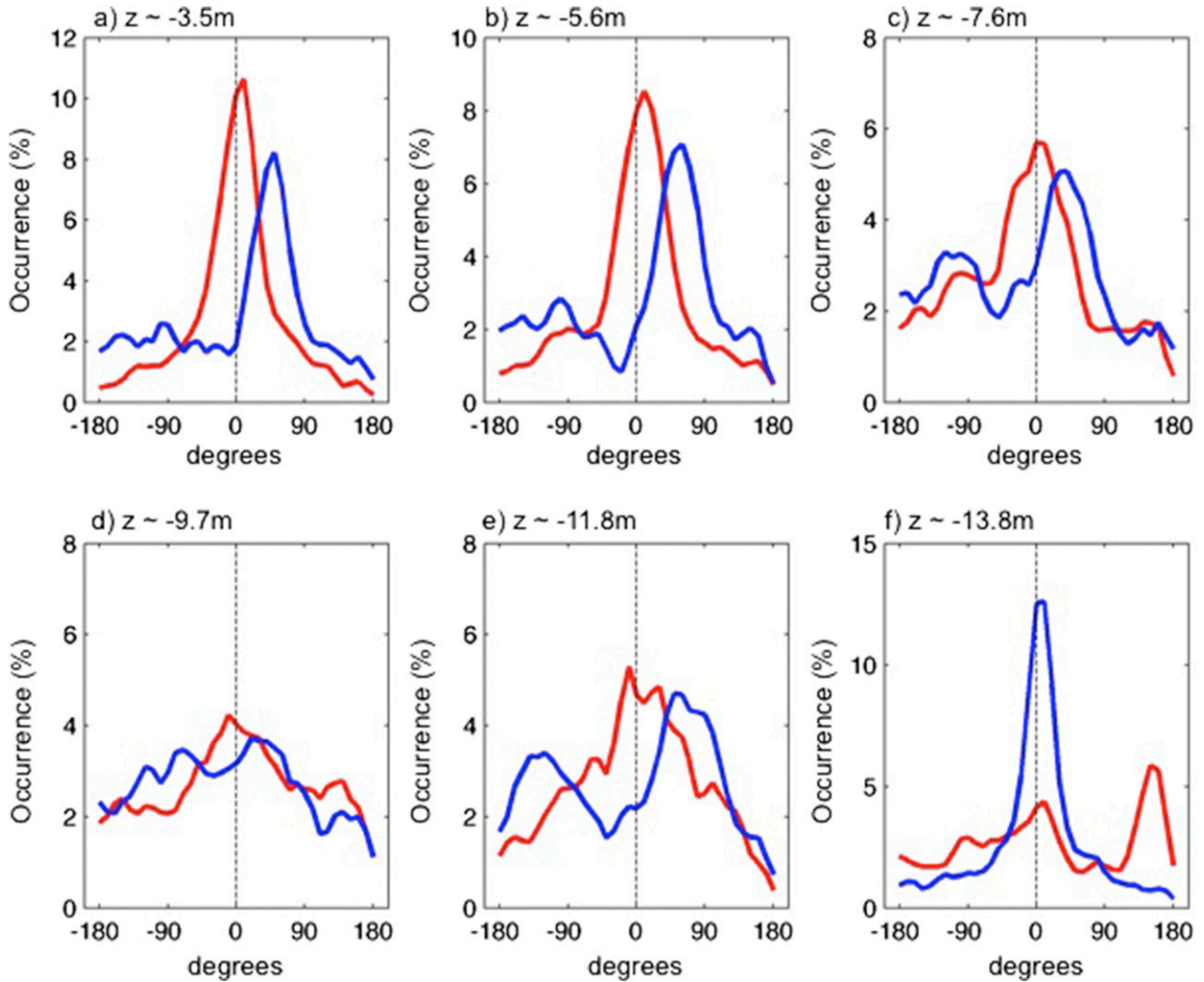
FIG. 10. The misalignment between the momentum flux vector and the surface wave direction (red line) and the local current direction (blue line), at depths of $z \sim$ (a) -3.5, (b) -5.6, (c) -7.6, (d) -9.7, (e) -11.8, and (f) -13.8 m. The local momentum flux is aligned with the surface waves through the majority of the water column (to a depth of $z \sim -11.8$ m), and only very near the bottom (within the bottom boundary layer) does the momentum flux align with the tidal currents.

APPENDIX

Uncertainties in Pressure Measurements

A main conclusion of this manuscript is that the primary mechanism by which energy from breaking waves is transmitted into the water column is through the work done by the covariance of turbulent pressure and velocity fluctuations. To support this conclusion, it is necessary to demonstrate that the observed pressure fluctuations are larger than the sensor noise level and not significantly contaminated by the dynamic pressure associated with flow distortion around the sensor. To better understand the potential sources of the observed pressure fluctuations, it is useful to examine the pressure equation derived for an inviscid fluid of constant density from the vertical momentum balance:

$$p = p_\eta + \rho g(\eta - z) + \rho \frac{\partial}{\partial t} \int_z^\eta w \, dz + \rho \frac{\partial}{\partial x_i} \int_z^\eta u_i w \, dz - \rho w^2,$$
$$(A1)$$

where the subscript η denotes evaluation at the ocean surface ($z = \eta$). In this form, the pressure consists of the value at the surface (first term on rhs), the hydrostatic contribution (second term on rhs), and the dynamic contributions of advective and local accelerations (third, fourth, and fifth terms on rhs).

The dynamic pressure terms contain both real pressure fluctuations caused by the local flow and accelerations in
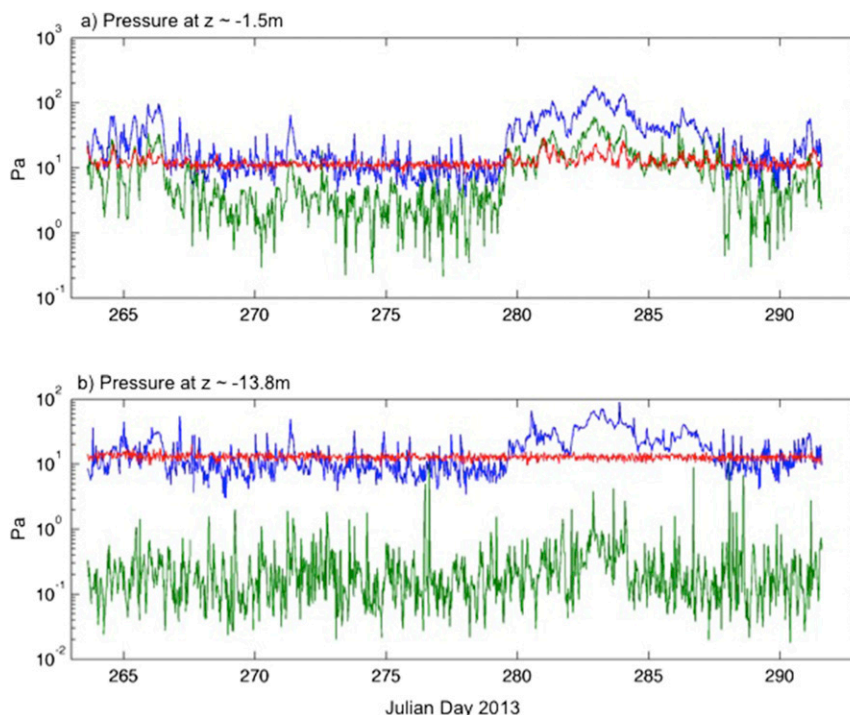
FIG. A1. Comparison of the RMS low-frequency ($<1/10$ Hz) pressure fluctuations (blue line), spectral estimate of instrument noise floor (red line), and the RMS low-frequency stagnation pressure calculated from the observed velocity (green line) following (A1) for $z \sim$ (a) -1.5 and (b) -13.8 m. Pressure measurements from $z \sim -13.8$ m were made not from the tower but from an adjacent bottom tripod.

the overlying water column, as well as potential errors associated with acceleration of the flow around the pressure housing. If the pressure sensor has a diameter d, the acceleration associated with the flow around the housing is $O(u^2/d)$, where u is the local velocity. However, this effect is limited to the region around the housing so that the integrated contribution to the pressure is $O(\rho u^2)$. This scaling is consistent with the Bernoulli relation and previous studies that use the stagnation pressure p_s as the upper bound on potential errors associated with flow distortion (Elliott 1972).

Here we estimate p_s as follows:

$$p_s = \frac{1}{2}\rho \langle u_j'^2 \rangle_{\text{RMS}}, \qquad (A2)$$

where the angled brackets denote a low-pass filter ($<1/10$ Hz) and we calculate the root-mean-square (RMS) value for each burst. We low-pass filter the sum of velocity fluctuations squared because we are only interested in the low-frequency pressure fluctuations. The value of p_s can be interpreted as the pressure error associated with complete flow stagnation at the sensor and is a plausible upper bound on the pressure error.

We begin by comparing the observed low-frequency ($<1/10$ Hz) pressure variability to the instrument noise floor (Fig. A1). The noise floor was estimated from the high-frequency (>10 Hz) pressure spectrum. A clear noise floor is observed in all pressure spectra (Fig. A2b), except under the most energetic conditions, and is consistent from burst to burst (~ 10 Pa). Under conditions of strong wind and wave forcing, the observed low-frequency pressure fluctuations exceed the instrument resolution by as much as an order of magnitude, both near the surface as well as near the bottom (Fig. A1).

At the pressure sensor 1.5 m below the mean water surface we observe low-frequency ($<1/10$ Hz) pressure fluctuations that are at least a factor of 3 larger than p_s (Fig. A1a). Most studies that have accurately measured the pressure error associated with flow distortion find that the total pressure error is typically on the order of 10% of p_s (Wyngaard et al. 1994). This would suggest that the pressure errors in our measurements are less than 5%. The low-frequency ($<1/10$ Hz) RMS pressure variations measured 0.7 m above the seabed ($z \sim -13.8$ m), from the sensor mounted on the tripod adjacent to the tower, are strongly correlated ($r^2 = 0.84$) with the pressure fluctuations observed near the surface
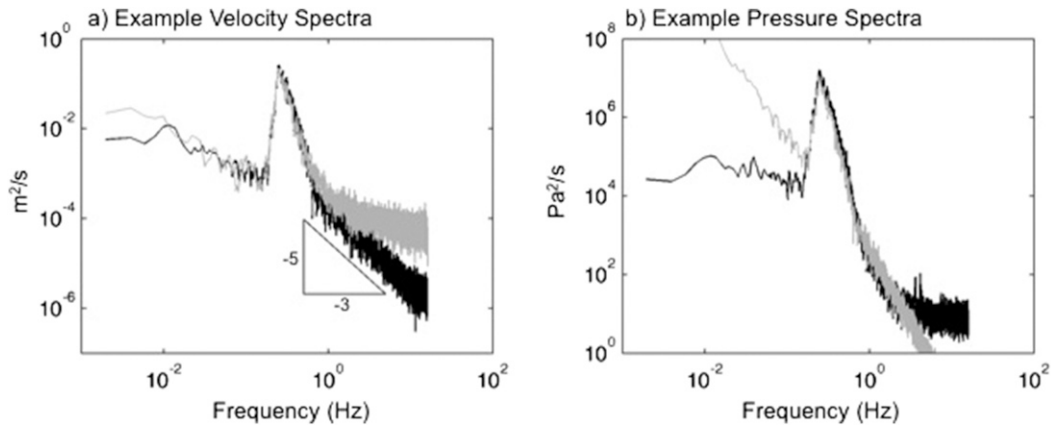
FIG. A2. Examples of (a) velocity and (b) pressure spectra measured at $z \sim -1.5\,\mathrm{m}$, which are typical of wave-dominated environments. In (a), the black line is the vertical velocity spectrum and the gray line is the spectrum of the horizontal component of velocity. A clear inertial ($-5/3$) range is evident to the right of the wave peak in the vertical velocity spectrum but is obscured by noise in the horizontal component. In (b), the black line is the observed pressure spectrum and the gray line is the pressure spectrum computed from the observed vertical velocity spectrum using linear wave theory [(A2)]. The agreement within the wave band is within 10% averaged over all bursts, suggesting only minor contamination of the pressure signal by flow distortion.

(Fig. A1b). Estimates of p_s exhibit little correlation between the surface and bottom ($r^2 = 0.13$). The lack of correlation in p_s and strong correlation in the observed pressure fluctuations throughout the water column is consistent with real pressure fluctuations.

In an attempt to further quantify the error in our measurements, we compare the observed pressure spectra to the theoretical pressure spectra based on linear wave theory:

$$S_{pp} = S_{ww} \frac{\rho^2 \omega^2}{k^2} \tanh^{-2}[k(z + H)], \qquad (A3)$$

where S_{ww} is the observed vertical velocity spectra and H is the water depth, ω is the radian frequency, and k is the wavenumber. Figure A2 shows an example of the observed pressure spectra, the corresponding pressure spectra derived from linear wave theory, and the corresponding velocity spectra. The velocity spectra show a pronounced wave peak separating the inertial subrange from the production scales of turbulence. At frequencies higher than the wave band, the horizontal velocity spectra become dominated by noise, obscuring the inertial subrange. Within the wave band, there is good agreement between the observed pressure spectra and linear wave theory. The agreement is quantified by integrating the variance in the wave band of the observed and predicted spectra. If we assume that all of the error between the observed and theoretical spectra is due to flow disturbance, the median pressure error for all bursts considered in this analysis is $\sim 10\%$. Within the wave band, the observed pressure spectra are larger than

predicted by linear wave theory on average, consistent with an increase in variance associated with flow disturbance. Herbers and Guza (1994) demonstrated that nonlinear interactions between surface waves elevate pressure spectra in the frequency range 0.3–0.7 Hz relative to linear wave theory, suggesting that 10% represents the upper bound on the uncertainty in our pressure measurements.

The above scaling arguments and calculations indicate that the errors in the pressure measurements are much smaller than the natural pressure fluctuations, at least at the temporal and spatial scales of interest, but the scalings and calculations do not answer the question of what causes the large natural pressure fluctuations that accomplish the observed pressure–velocity covariance. Our uppermost measurement of velocity is at $z \sim -1.5\,\mathrm{m}$, and we do not resolve the velocities immediately beneath the ocean surface. Breaking waves have been shown to result in large accelerations in this region (Dommermuth et al. 1988; Chang and Liu 1998), which would contribute to the pressure fluctuations observed at the sensors lower in the water column. A simple scaling for acceleration under breaking waves suggests that $u^2 = O(\omega^2 H_s^2)$, so that $p = O(\rho \omega^2 H_s^2)$. This estimate is an order of magnitude larger than p_s and is generally consistent with the magnitude of the pressure fluctuations that we observe (e.g., Fig. 8). We hypothesize that the large pressure fluctuations we observed throughout the water column are the result of large accelerations very near the ocean surface, not resolved by our velocity measurements.

REFERENCES

Abry, P., S. Fauve, P. Flandrin, and C. Laroche, 1994: Analysis of pressure fluctuations in swirling turbulent flows. *J. Phys. II*, **4**, 725–733.

Agrawal, Y. C., E. A. Terray, M. A. Donelan, P. A. Hwang, A. J. Williams III, W. M. Drennan, K. K. Kahma, and S. A. Kitaigorodskii, 1992: Enhanced dissipation of kinetic energy beneath surface waves. *Nature*, **359**, 219–220, doi:10.1038/359219a0.

Anis, A., and J. N. Moum, 1995: Surface wave–turbulence interactions: Scaling $\varepsilon(z)$ near the sea surface. *J. Phys. Oceanogr.*, **25**, 2025–2045, doi:10.1175/1520-0485(1995)025<2025:SWISNT>2.0.CO;2.

Burchard, H., 2001: Simulating the wave-enhanced layer under breaking surface waves with two equation turbulence models. *J. Phys. Oceanogr.*, **31**, 3133–3145, doi:10.1175/1520-0485(2001)031<3133:STWELU>2.0.CO;2.

Cao, N., S. Chen, and G. D. Doolen, 1999: Statistics and structures of pressure in isotropic turbulence. *Phys. Fluids*, **11**, 2235–2250, doi:10.1063/1.870085.

Chang, K. A., and P. L. F. Liu, 1998: Velocity, acceleration and vorticity under a breaking wave. *Phys. Fluids*, **10**, 327–329, doi:10.1063/1.869544.

Craig, P. D., and M. L. Banner, 1994: Modeling wave-enhanced turbulence in the ocean surface layer. *J. Phys. Oceanogr.*, **24**, 2546–2559, doi:10.1175/1520-0485(1994)024<2546:MWETIT>2.0.CO;2.

Dommermuth, D. G., D. K. Yue, W. M. Lin, R. J. Rapp, E. S. Chan, and W. K. Melville, 1988: Deep-water plunging breakers: A comparison between potential theory and experiments. *J. Fluid Mech.*, **189**, 423–442, doi:10.1017/S0022112088001089.

Donelan, M. A., and W. J. Pierson, 1987: Radar scattering and equilibrium ranges in wind-generated waves with application to scatterometry. *J. Geophys. Res.*, **92**, 4971–5029, doi:10.1029/JC092iC05p04971.

Douady, S., Y. Couder, and M. E. Brachet, 1991: Direct observations of the intermittency of intense vorticity filaments in turbulence. *Phys. Rev. Lett.*, **67**, 983–986, doi:10.1103/PhysRevLett.67.983.

Drennan, W. M., M. A. Donelan, E. A. Terray, and K. B. Katsaros, 1996: Oceanic turbulence dissipation measurements in SWADE. *J. Phys. Oceanogr.*, **26**, 808–815, doi:10.1175/1520-0485(1996)026<0808:OTDMIS>2.0.CO;2.

Elliott, J. A., 1972: Instrumentation for measuring static pressure fluctuations within the atmospheric boundary layer. *Bound.-Layer Meteor.*, **2**, 476–495, doi:10.1007/BF00821550.

Fauve, S., C. Laroche, and B. Castaing, 1993: Pressure fluctuations in swirling turbulent flows. *J. Phys. II*, **3**, 271–278.

Feddersen, F., J. H. Trowbridge, and A. J. Williams III, 2007: Vertical structure of dissipation in the nearshore. *J. Phys. Oceanogr.*, **37**, 1764–1777, doi:10.1175/JPO3098.1.

Fisher, A. W., L. P. Sanford, and S. E. Suttles, 2015: Wind stress dynamics in Chesapeake Bay: Spatiotemporal variability and wave dependence in a fetch-limited environment. *J. Phys. Oceanogr.*, **45**, 2679–2696, doi:10.1175/JPO-D-15-0004.1.

Gemmrich, J., 2010: Strong turbulence in the wave crest region. *J. Phys. Oceanogr.*, **40**, 583–595, doi:10.1175/2009JPO4179.1.

Gerbi, G. P., J. H. Trowbridge, J. B. Edson, A. J. Plueddemann, E. A. Terray, and J. J. Fredericks, 2008: Measurements of momentum and heat flux across the air–sea interface. *J. Phys. Oceanogr.*, **38**, 1054–1072, doi:10.1175/2007JPO3739.1.

——, ——, E. A. Terray, A. J. Plueddemann, and T. Kukulka, 2009: Observations of turbulence in the ocean surface boundary layer: Energetics and transport. *J. Phys. Oceanogr.*, **39**, 1077–1096, doi:10.1175/2008JPO4044.1.

Grachev, A. A., C. W. Fairall, J. E. Hare, J. B. Edson, and S. D. Miller, 2003: Wind stress vector over ocean waves. *J. Phys. Oceanogr.*, **33**, 2408–2429, doi:10.1175/1520-0485(2003)033<2408:WSVOOW>2.0.CO;2.

Herbers, T. H. C., and R. T. Guza, 1994: Nonlinear wave interactions and high-frequency seafloor pressure. *J. Geophys. Res.*, **99**, 10 035–10 048, doi:10.1029/94JC00054.

Janssen, P. A. E. M., 1999: On the effect of ocean waves on the kinetic energy balance and consequences for the inertial dissipation technique. *J. Phys. Oceanogr.*, **29**, 530–534, doi:10.1175/1520-0485(1999)029<0530:OTEOOW>2.0.CO;2.

Kaimal, J. C., J. C. Wyngaard, Y. Izumi, and O. R. Cote, 1972: Spectral characteristics of surface-layer turbulence. *Quart. J. Roy. Meteor. Soc.*, **98**, 563–589, doi:10.1002/qj.49709841707.

Kenyon, K. E., 1969: Stokes drift for random gravity waves. *J. Geophys. Res.*, **74**, 6991–6994, doi:10.1029/JC074i028p06991.

Kitaigorodskii, S. A., 1983: On the theory of the equilibrium range in the spectrum of wind-generated gravity waves. *J. Phys. Oceanogr.*, **13**, 816–827, doi:10.1175/1520-0485(1983)013<0816:OTTOTE>2.0.CO;2.

Lumley, J., and E. Terray, 1983: Kinematics of turbulence convected by a random wave field. *J. Phys. Oceanogr.*, **13**, 2000–2007, doi:10.1175/1520-0485(1983)013<2000:KOTCBA>2.0.CO;2.

McBean, G. A., and J. A. Elliott, 1975: The vertical transports of kinetic energy by turbulence and pressure in the boundary layer. *J. Atmos. Sci.*, **32**, 753–766, doi:10.1175/1520-0469(1975)032<0753:TVTOKE>2.0.CO;2.

McWilliams, J. C., P. P. Sullivan, and C.-H. Moeng, 1997: Langmuir turbulence in the ocean. *J. Fluid Mech.*, **334**, 1–30, doi:10.1017/S0022112096004375.

——, E. Huckle, J. H. Liang, and P. P. Sullivan, 2012: The wavy Ekman layer: Langmuir circulations, breaking waves, and Reynolds stress. *J. Phys. Oceanogr.*, **42**, 1793–1816, doi:10.1175/JPO-D-12-07.1.

Melville, W. K., 1996: The role of surface-wave breaking in air–sea interaction. *Annu. Rev. Fluid Mech.*, **28**, 279–321, doi:10.1146/annurev.fl.28.010196.001431.

——, F. Veron, and C. White, 2002: The velocity field under breaking waves: Coherent structures and turbulence. *J. Fluid Mech.*, **454**, 203–233, doi:10.1017/S0022112001007078.

Metais, O., and M. Lesieur, 1992: Spectral large-eddy simulation of isotropic and stably stratified turbulence. *J. Fluid Mech.*, **239**, 157–194, doi:10.1017/S0022112092004361.

Mitsuyasu, H., 1985: A note on the momentum transfer from wind to waves. *J. Geophys. Res.*, **90**, 3343–3345, doi:10.1029/JC090iC02p03343.

Pizzo, N. E., and W. K. Melville, 2013: Vortex generation by deep-water breaking waves. *J. Fluid Mech.*, **734**, 198–218, doi:10.1017/jfm.2013.453.

Rapp, R. J., and W. K. Melville, 1990: Laboratory measurements of deep-water breaking waves. *Philos. Trans. Roy. Soc. London*, **A331**, 735–800, doi:10.1098/rsta.1990.0098.

Rieder, K. F., J. A. Smith, and R. A. Weller, 1994: Observed directional characteristics of the wind, wind stress, and surface waves on the open ocean. *J. Geophys. Res.*, **99**, 22 589–22 596, doi:10.1029/94JC02215.

Scully, M. E., A. W. Fisher, S. E. Suttles, L. P. Sanford, and W. C. Boicourt, 2015: Characterization and modulation of Langmuir circulation in Chesapeake Bay. *J. Phys. Oceanogr.*, **45**, 2621–2639, doi:10.1175/JPO-D-14-0239.1.

She, Z.-S., E. Jackson, and S. A. Orszag, 1990: Intermittent vortex structures in homogeneous isotropic turbulence. *Nature*, **344**, 226–228, doi:10.1038/344226a0.

Sullivan, P. P., J. C. McWilliams, and W. K. Melville, 2007: Surface gravity wave effects in the oceanic boundary layer: Large-eddy simulation with vortex force and stochastic breakers. *J. Fluid Mech.*, **593**, 405–452, doi:10.1017/S002211200700897X.

Terray, E. A., M. A. Donelan, Y. C. Agrawal, W. M. Drennan, K. K. Kahma, A. J. Williams III, P. A. Hwang, and S. A. Kitaigorodskii, 1996: Estimates of kinetic energy dissipation under breaking waves. *J. Phys. Oceanogr.*, **26**, 792–807, doi:10.1175/1520-0485(1996)026<0792:EOKEDU>2.0.CO;2.

Trowbridge, J. H., 1998: On a technique for measurement of turbulent Reynolds stress in the presence of surface waves. *J. Atmos. Oceanic Technol.*, **15**, 290–298, doi:10.1175/1520-0426(1998)015<0290:OATFMO>2.0.CO;2.

Wilczak, J., S. Oncley, and S. Stage, 2001: Sonic anemometer tilt correction algorithms. *Bound.-Layer Meteor.*, **99**, 127–150, doi:10.1023/A:1018966204465.

Wyngaard, J. C., and O. R. Cote, 1972: Cospectral similarity in the atmospheric surface layer. *Quart. J. Roy. Meteor. Soc.*, **98**, 590–603, doi:10.1002/qj.49709841708.

——, A. Siegel, and J. M. Wilczak, 1994: On the response of a turbulent-pressure probe and the measurement of pressure transport. *Bound.-Layer Meteor.*, **69**, 379–396, doi:10.1007/BF00718126.